Inorganic Chemistry

Article

pubs.acs.org/IC

Halogen Oxidation and Halogen Photoelimination Chemistry of a Platinum−Rhodium Heterobimetallic Core

Timothy R. Cook, Brian D. McCarthy, Daniel A. Lutterman, and Daniel G. Nocera*

Department of Chemistry, 6-335, Massachusetts Institute of Technology, 77 Massachusetts Avenue, Cambridge, Massachusetts 02139-4307, United States

Supporting Information

ABSTRACT: The heterobimetallic complexes, PtRh(tfepma)$_2$(CN^{t}Bu)X$_3$ (X = Cl, Br), are assembled by the treatment of Pt(cod)X$_2$ (cod =1,5-cyclooctadiene) with {Rh(cod)X}$_2$, in the presence of *tert*-butylisonitrile (CN^{t}Bu) and tfepma (tfepma = bis(trifluoroethoxyl)phosphinomethylamine). The neutral complexes contain Pt−Rh single bonds with metal−metal separations of 2.6360(3) and 2.6503(7) Å between the square planar Pt and octahedral Rh centers for the Cl and Br complexes, respectively. Oxidation of the XPt^{I}Rh^{II}X$_2$ cores with suitable halide sources (PhICl$_2$ or Br$_2$) furnishes PtRh(tfepma)$_2$(CN^{t}Bu)X$_5$, which preserves a Pt−Rh bond. For the chloride system, the initial oxidation product orients the platinum-bound chlorides in a *meridional* geometry, which slowly transforms to a *facial* arrangement in pentane solution as verified by X-ray crystal analysis. Irradiation of the *mer*- or *fac*-Cl$_3$Pt^{III}Rh^{II}Cl$_2$ isomers with visible light in the presence of olefin promotes the photoelimination of halogen and regeneration of the reduced ClPt^{I}Rh^{II}Cl$_2$ core. In addition to exhibiting photochemistry similar to that of the chloride system, the oxidized bromide cores undergo thermal reduction chemistry in the presence of olefin with zeroth-order olefin dependence. Owing to an extremely high photoreaction quantum yield for the *fac*-ClPt^{I}Rh^{II}Cl$_2$ isomer, details of the X$_2$ photoelimination have been captured by transient absorption spectroscopy. We now report the first direct observation of the photointermediate that precedes halogen reductive elimination. The intermediate is generated promptly upon excitation (<8 ns), and halogen is eliminated from it with a rate constant of 3.6×10^4 s^{-1}. As M−X photoactivation and elimination is the critical step in HX splitting, these results establish a new guidepost for the design of HX splitting cycles for solar energy storage.

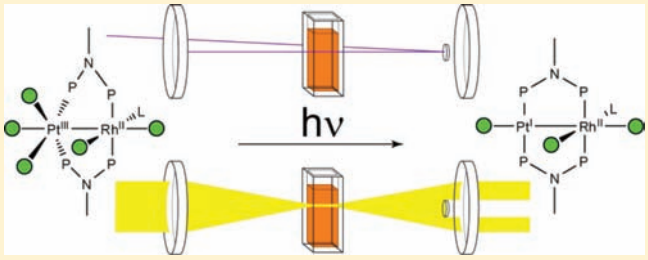

INTRODUCTION

Inorganic chemistry is a central subject to the conversion and storage of solar energy.[1] Whereas solar energy provides a promising energy source of sufficient scale to meet future energy needs,[2,3] its implementation would benefit from a highly distributed storage medium.[4−6] The use of sunlight to drive the formation of hydrogen as a chemical fuel from readily available substrates such as HX (X = Cl, Br, OH)[1,7] emerges as a logical storage medium owing to its high energy density.[4] Recent advances have led to the development of new water-splitting catalysts,[8−29] and a detailed understanding of the mechanism of water splitting[30−41] has led to new technological targets such as the artificial leaf.[42−44] Conversely, much less is known about the mechanism of HX splitting although it is a simpler chemical process involving only two electrons and two protons as opposed to the 4e$^-$−4H$^+$ process of water splitting.[7,45,46] The slower progress in the area of HX splitting underscores the lack of mechanistic understanding of the 2e$^-$−2H$^+$ process of the HX transformation.

Direct photon-to-fuel hydrogen photocatalysis can be achieved by the cycle shown in Scheme 1. Whereas hydrogen production subsequent to HX addition occurs with facility,[7] the strong M−X bond is recalcitrant to activation.[45] Hence, the overall efficiency for the H$_2$ photocycle shown in Scheme 1 is limited by the efficiency of halogen photoelimination, thereby providing an imperative for an improved understanding of how to activate M−X bonds. Although reductive elimination is a standard reaction type of coordination and organometallic chemistry, reductive elimination of halogen from metal centers is unusual.[47−49] The elimination reaction is thermodynamically unfavorable, and even if the energetics can be overcome with the input of a photon, the reaction must be driven by halogen trapping since the back-reaction is facile and favorable.[50−53] Only recently has photochemical X$_2$ reductive elimination by

Scheme 1

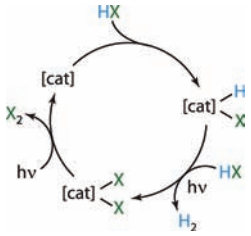

Received: January 1, 2012
Published: April 4, 2012

   dx.doi.org/10.1021/ic300004x | *Inorg. Chem.* 2012, 51, 5152−5163

transition-metal complexes been demonstrated by irradiation in the solid state of homobimetallic $Pt_2(tfepma)_2Cl_6$ (tfepma = bis(trifluoroethoxyl)phosphinomethylamine) and mono- and homobimetallic nickel[54] and gold phosphine complexes.[55−59] High quantum yields for halogen photoelimination permit M−X bond activation to be effected in the solid state.[58,59] The homobimetallic Pt_2 and Au_2 complexes provide the first examples of trap-free X_2 reductive elimination and the first authentic examples of energy storage via M−X bond activation because the gaseous photoproduct is readily separated from the photoreduced metal product, thus removing the possibility of a bimolecular back-reaction.

Motivated by the H_2 photoelimination chemistry of Rh_2 bimetallic cores and the X_2 photoelimination chemistry of Pt_2 bimetallic cores, we have turned our attention to the chemistry of PtRh heterobimetallic complexes. Our interest in this class of compounds stems from a desire to strike a balance between the H_2 and X_2 photoelimination chemistry needed to effect the photocycle in Scheme 1. Bimetallic PtRh complexes assume a coordination geometry that contrasts the face-to-face square planar, otherwise known as 4:4, coordination environment that is characteristic of homobimetallics.[60−68] A 3:5 isomeric coordination environment may prevail for heterobimetallic complexes comprising late transition metals (see Scheme 2).[69−71]

Scheme 2

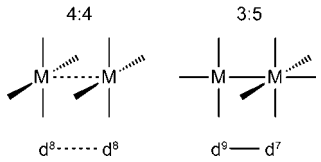

Balch and co-workers suggested that the inherent asymmetry of the metal−metal core in heterobimetallic complexes assists the 3:5 coordination environment. This contention is further supported by the observation that two-electron mixed valence complexes of homobimetallic centers have been isolated when an asymmetry is electronically induced by the coordinating ligands. For group 9 bimetallic centers, for example, two-electron mixed valency is the rule rather than the exception when the bridging ligands contain an acceptor−donor−acceptor motif capable of asymmetric π bonding.[1,50,72−76] When this electronic asymmetry is removed, by replacing the nitrogen of the P−N−P backbone of the tfepma ligand with a methylene spacer, the 4:4 valence symmetric product, $Rh_2^{I,I}(tfepm)_3Cl_2$ (tfepm = bis(trifluoroethoxyl)phosphinomethane), is isolated. For the purposes of HX splitting, the 3:5 coordination environment is desirable insofar as the electronic structure is dominated by a direct metal−metal interaction; the metal−metal bond in complexes of this type can be used as a chromophore to drive photoelimination chemistry from the $d\sigma^*$ excited states.[77] In contrast, weakly interacting metal cores as found in 4:4 complexes and related $d^8\cdots d^{10}$ complexes are typically luminescent,[78,79] as are monomeric Pt and dinuclear Pt_2 and Rh_2 complexes.[80−83] An emissive excited state is undesirable because luminescence is a chemically nonproductive excited-state relaxation pathway.

Both 3:5 and 4:4 coordination environments prevail for PtRh heretobimetallics;[69] the 3:5 complexes are typically cationic and possess neutral donor ligands about the metal centers. Despite a well-documented structural chemistry, a redox chemistry for $Pt^{II}Rh^{I}$ and related $Pt^{I}Rh^{II}$ cores is conspicuously absent. Moreover, a well-defined two-electron photochemistry of relevance to Scheme 1 has yet to be defined. Here we report the synthesis and structure of a tfepma-bridged $XPt^{I}Rh^{II}X_2$ heterobimetallic core, which undergoes two-electron oxidation to yield an $X_3Pt^{III}Rh^{II}X_2$ core in two isomeric forms when X = Cl and a single product when X = Br. Halogen elimination from both $Cl_3Pt^{III}Rh^{II}Cl_2$ cores is photoinduced at exceptionally high efficiency, so much so, that the photochemistry can be initiated by a laser and the process of M—X activation may be probed by time-resolved spectroscopy.

EXPERIMENTAL SECTION

General Considerations. All solvents were reagent grade or better and were obtained commercially and dried by passage through an alumina column. Chemical manipulations were performed in a nitrogen-filled glovebox. $\{Rh(cod)Cl\}_2$ (98%), $Pt(cod)Cl_2$ (98%), and $Pt(cod)Br_2$ (98%) were obtained from Strem Chemicals. $\{Rh(cod)Br\}_2$ was prepared by adapting the reported synthesis of $\{Rh(cod)Cl\}_2$ to the analogous bromide reagents.[84] CN^{t}Bu, 2,3-dimethyl-1,3-butadiene (DMBD, 98%), and 1-hexene (99+%) were obtained from Sigma-Aldrich. $PhICl_2$,[85] tfepma,[86] and potassium ferrioxalate[87] were prepared by literature methods. Deuterated solvents for ^{1}H NMR spectroscopy (CD_3CN, 99.8%; CD_2Cl_2, 99.9%; C_6D_6, 99.5%) were purchased from Cambridge Isotope Laboratories, Inc. (Andover, MA).

Preparation of $PtRh(tfepma)_2(CN^tBu)Cl_3$ (1). To $\{Rh(cod)Cl\}_2$ (59 mg, 0.12 mmol) dissolved in 5 mL of THF, was added dropwise tfepma (231 mg, 0.474 mmol) in ∼1 mL of THF followed by a solution of CN^{t}Bu (30 mg, 0.36 mmol) in ∼1 mL THF. After the solution stirred for 5 min, $Pt(cod)Cl_2$ (89 mg, 0.24 mmol) was added as a solid, and the solution was stirred overnight, resulting in a clear-yellow solution. THF was removed under reduced pressure, and the resulting solid was washed with pentane to yield a yellow solid. Yield: 242 mg (0.166 mmol, 69%). Crystals suitable for X-ray diffraction were grown from pentane-layered CH_2Cl_2 solutions. $^{31}P\{^1H\}$ NMR (CH_2Cl_2) δ/ppm: 123.15 (m, $^1J_{Pt-P}$ = 4365.5 Hz), 112.6 (m). ^{1}H NMR (CD_3CN) δ/ppm: 1.45 (s, 9 H), 2.90 (m, 6 H), 4.63−5.17 (br, 16 H). λ_{max}/nm (ε/M^{-1} cm^{-1}) in CH_3CN: 281 (24,800); 372 br (3,600); 433 sh (800). Elem. Anal. Calcd for PtRh C, 18.90; H, 2.14; Cl, 7.28; F, 31.19; N, 2.87; O, 8.76; P, 8.48; Pt, 13.35; Rh, 7.04. Found: C, 18.99; H, 2.12; N, 2.92.

Preparation of *trans*-$PtRh(tfepma)_2(CN^tBu)Cl_5$ (2). A solution of $PhICl_2$ (45 mg, 0.16 mmol) in 2 mL of CH_2Cl_2 was added dropwise to a solution of **1** (217 mg, 0.148 mmol) in 5 mL of CH_2Cl_2 to prompt an immediate color change from yellow to orange. The CH_2Cl_2 was removed under reduced pressure and the resulting material washed with pentane and dried to yield an orange solid. Yield: 167 mg (0.109 mmol, 73%). Crystals suitable for X-ray diffraction were grown from pentane-layered CH_2Cl_2 solutions. $^{31}P\{^1H\}$ NMR (CH_2Cl_2) δ/ppm: 64.45 (m, $^1J_{Pt-P}$ = 2929.2 Hz), 101.0 (m). ^{1}H NMR ($CDCl_3$) δ/ppm: 1.50 (s, 9 H), 3.04 (m, 6 H), 4.65−5.51 (br, 16 H). λ_{max}/nm (ε/M^{-1} cm^{-1}) in CH_3CN: 281 (11,900); 327 (14,100); 367 (20,800). Elem. Anal. Calcd for **2**: C, 18.02; H, 2.04; Cl, 11.57; F, 29.75; N, 2.74; O, 8.35; P, 8.08; Pt, 12.73; Rh, 6.71. Found: C, 18.37; H, 2.14; N, 2.93.

Preparation of *cis*-$PtRh(tfepma)_2(CN^tBu)Cl_5$ (3). A solution of $PhICl_2$ (63 mg, 0.23 mmol) in 2 mL of CH_2Cl_2 was added rapidly to a solution of **1** (217 mg, 0.142 mmol) in 5 mL of CH_2Cl_2 to prompt an immediate color change from a yellow to orange. The solvent was removed in vacuo, and the resulting solid was treated with pentane. The saturated pentane solution was allowed to stand overnight, during which time orange needles of **3** deposited from solution. The pentane was decanted, and the crystals were dried in vacuo. Yield: 128 mg (0.0835 mmol, 56%). Crystals suitable for X-ray diffraction were collected from the initial isolated material. $^{31}P\{^1H\}$ NMR (CH_2Cl_2) δ/ppm: 46.5 (m, $^1J_{Pt-P}$ = 4319.0 Hz), 103.8 (m). ^{1}H NMR ($CDCl_3$) δ/ppm: 1.56 (s, 9 H), 3.08 (m, 6 H), 4.35−5.33 (br, 16 H). λ_{max}/nm (ε/M^{-1} cm^{-1}) in CH_3CN: 278 (12,400); 366 (16,000); 468 (4,300). Elem. Anal. Calcd for **3**: C, 18.02; H, 2.04; Cl, 11.57; F, 29.75; N, 2.74; O, 8.35; P, 8.08; Pt, 12.73; Rh, 6.71. Found: C, 18.20; H, 2.11; N, 2.80.

dx.doi.org/10.1021/ic300004x | Inorg. Chem. 2012, 51, 5152−5163

Preparation of PtRh(tfepma)$_2$(CN^{t}Bu)Br$_3$ (4). To a scintillation vial was added 0.100 g (0.172 mmol) of {Rh(cod)Br}$_2$ followed by 4 mL of CH_2Cl_2. To this solution was added 0.335 g (0.688 mmol) of tfepma dissolved in 3 mL CH_2Cl_2 followed by 0.043 g (0.517 mmol) of ^{t}BuNC dissolved in 2 mL CH_2Cl_2 during which the orange solution turned deep purple-red before becoming a clear orange color after 30 s. To this solution was added 0.159 g (0.343 mmol) of Pt(cod)Br$_2$ as a solid and the resulting mixture allowed to stir for 4 h during which time the Pt(cod)Br$_2$ dissolved, and a yellow-orange solution resulted. The CH_2Cl_2 was removed in vacuo to give a yellow solid which was washed with pentane and dried to give **4** as a yellow powder. Yield: 0.387 g (0.243 mmol, 70%). Crystals suitable for X-ray diffraction were grown from pentane-layered CH_2Cl_2 solution. ^{1}H NMR (CD_2Cl_2) δ/ppm: 1.43 (s, 6 H), 1.44 (s, 3 H) 2.89 (m, 6 H), 4.52−5.08 (br, 16 H). ^{31}P{^{1}H} NMR (CD_2Cl_2) δ/ppm: 111.74 (m, $^1J_{Pt-P}$ = 7147.5 Hz), 110.14 (m). λ_{max}/nm (ε/M^{-1} cm^{-1}) in CH_3CN: 299 (24,300); 386 br (3,880). Elem. Anal. Calcd for **3**: C, 17.32; H, 1.96; N, 2.74; Found: C, 18.16; H, 2.12; N, 2.85.

Preparation of PtRh(tfepma)$_2$(CN^{t}Bu)Br$_5$ (5). A solution of **4** was made by dissolving 0.118 g (0.0740 mmol) of the yellow solid in 5 mL CH_2Cl_2. To this solution was added an 0.384 mL aliquot of 0.198 M Br_2 in CH_2Cl_2. The Br_2 solution was made by diluting 0.05 mL of Br_2 to 5 mL total volume with CH_2Cl_2. The yellow solution immediately turned a deep-red color upon addition of Br_2. After 15 min of stirring at room temperature the CH_2Cl_2 was removed in vacuo to give **5** as a microcrystalline deep-red solid. Yield: 0.112 g (0.0640 mmol, 86%). Crystals suitable for X-ray diffraction were grown from concentrated CH_2Cl_2 solutions stored at −20 °C for 24 h. ^{1}H NMR (CD_2Cl_2) δ/ppm: 1.48 (s, 6 H), 1.50 (s, 3 H) 3.01 (m, 6 H), 4.62−5.40 (br, 16 H). ^{31}P{^{1}H} NMR (CD_2Cl_2) δ/ppm: 47.86 (m, $^1J_{Pt-P}$ = 4829.2 Hz), 71.69 (m). λ_{max}/nm (ε/M^{-1} cm^{-1}) in CH_3CN: 270 (20,000); 365 (19,200); 434 (15,500). Elem. Anal. Calcd. for **3**: C, 15.74; H, 1.78; N, 2.74. Found: C, 16.09; H, 1.94; N, 2.42.

Physical Methods. Extinction coefficients were determined using six solutions per compound at varying concentrations. The maximum absorptions of the solutions ranged from 0.15 to 1.2 as measured on an Agilent 8453 UV−visible photodiode array spectrometer for compounds **1**-**3** and a Varian Cary 5000 UV−vis−NIR spectrometer for compounds **4** and **5**. The molar absorptivity was determined for each solution using Beer's Law, and the reported extinction coefficients were taken as the average of the six solutions. UV−vis spectra for photochemical experiments were recorded on a S. I. Photonics, CCD Array UV−vis spectrophotometer. NMR spectra were recorded on a Varian 300 or Varian Inova-500 NMR spectrometer. ^{1}H NMR spectra were referenced to the proteo impurities of the solvent and ^{31}P{^{1}H} spectra were referenced to an external 85% D_3PO_4 standard with positive chemical shifts reported to the higher frequency of the reference. Elemental analysis was performed by Midwest Microlabs, LLc.

Photochemistry. Preparation for UV−vis photolysis and quantum yields were conducted in a nitrogen-filled glovebox. 1-hexene and DMBD were degassed by freeze−pump−thaw, and samples were maintained air-free for the duration of each experiment. Light from an Oriel 1000 W, Hg/Xe arc lamp was passed through a collimating lens and an iris to give a ∼1 cm diameter beam. Suitable combinations of long pass filters to remove the high energy ultraviolet light and Hg line filters for wavelength selection were employed. Quantum yield measurements for the conversion **2** and **3** to **1** were performed in triplicate and measured over a range of trap concentrations using potassium ferrioxalate as an actinometer.[87] Solutions of **3** with 1.0, 0.5, and 0.1 M DMBD were prepared in the dark to prevent ambient light from inducing photolysis. Solutions of **2** were stable to ambient light over the time scale of the quantum yield experiments so no additional measures were needed to safeguard the sample from light during sample preparation and manipulation. Samples for photolysis on the NMR scale were irradiated in J-Young tubes and samples for quantum yields and UV−vis monitored photolysis were kept in sealed quartz cuvettes with stir bars; for both types of experiments, the photolysis vessel was placed in a 20 °C recirculating water bath.

Thermal Kinetics. A Varian Inova-500 NMR spectrometer was used to monitor thermal reduction kinetics by ^{31}P{^{1}H}. Triphenylphosphate (22 μmol) was used as an internal integration standard. **5** (22 mg, 13 μmol) was dissolved in acetonitrile and the volume increased to 1 mL by adding 2,3-dimethyl-1,3-butadiene. A collection time of 153 s and a delay time of 120 s were used.

Transient Spectroscopy. Solutions of **3** in acetonitrile with degassed olefin were prepared in 500-mL Schlenk flasks in an N_2 filled glovebox. Solutions were flowed through a 3-mm diameter, 1-cm path length flow cell (Starna, Type 585.2) using a peristaltic pump and positive argon flow into a second Schlenk flask. Nanosecond transient absorption (TA) measurements were made with the pump light provided by the third harmonic (355 nm) of a Quanta-Ray Nd:YAG laser (Spectra-Physics) running at 10 Hz. Probe white light was provided by a 75 W Xe-arc lamp (Photon Technologies Inc.). The signal light passed through a Triax 320 spectrometer, where it was dispersed by a 300 nm × 250 nm blazed grating and collected with either an intensified gated CCD camera (ICCD, CCD 30-11, Andor Technology, 1024 × 256 pixels, 26 μm^2) for TA spectra or a photomultiplier tube (PMT) for TA single-wavelength kinetics. PMT outputs were collected and averaged with a 1 GHz oscilloscope (LeCroy 9384CM). A TTL pulse synchronized with the Q-switch of the Infinity laser was delayed 99 ms before triggering the shutter for the probe light. Electronic delays were created with SRS DG535 delay generators (Stanford Research Systems). These delay boxes, in combination with electronic shutters (Uniblitz), were used to create the necessary pulse sequence.[88]

X-ray Crystallography. **1** was crystallized from CH_2Cl_2 solutions layered with pentane, crystallization of **2** was induced by the slow evaporation of CH_2Cl_2 solutions, and **3** was crystallized by allowing saturated pentane solutions of **2** to stand overnight. **4** and **5** were crystallized by layering pentane over a CH_2Cl_2 solution and cooling to −20 °C. For each species, single crystals were immersed in a drop of Paratone N oil on a clean microscope slide, affixed to a loop and then cooled to 100 K. The crystals were mounted on a Bruker three-circle goniometer platform equipped with an APEX detector. A graphite monochromator was employed for wavelength selection of the Mo K_α radiation (λ = 0.71073 Å). The data were processed and refined using the program SAINT supplied by Siemens Industrial Automation Inc. Structures were solved by a Patterson heavy atom map and refined by standard difference Fourier techniques in the *SHELXTL* program suite (6.10 v., Sheldrick G. M., and Siemens Industrial Automation, Inc., 2000).[89] Hydrogen atoms were placed in calculated positions using the standard riding model and refined isotropically; all other atoms were refined anisotropically. Positional disorder of the trifluoroethoxy groups of the tfepma ligands and the CN^{t}Bu ligand of **1** was modeled. The 1−2 distances of disordered parts of **2** were restrained to be similar using the SAME command. Anisotropic parameter (SIMU) and rigid bond (DELU) restraints were then applied to the structure. These restraints were also used, along with the SAME and EADP restraints to model the disorder of the CN^{t}Bu ligand of **3**. The refinement of **4** required both SIMU and DELU restraints to resolve solvent disorder of a CH_2Cl_2 molecule. The structure of **5** required global SIMU and DELU restraints in addition to restraining the 1,2 and 1,3 distances of CH_2Cl_2 solvent molecules to be similar. Significant disorder of the $-OCH_2CF_3$ arms of the tfepma ligands required an ISOR restraint on C101 and C203. The significant disorders in this structure are responsible for the alerts found in the checkCIF report.

Computational Analysis. All calculations were performed using the *Gaussian03* (G03) program package,[90] with the Becke three-parameter hybrid exchange and the Lee−Yang−Parr correlation functionals (B3LYP).[91−93] The 6-31G* basis set was used for H, C, N, P, F, and Cl,[94] along with the Stuttgart/Dresden (SDD) energy-consistent pseudopotentials for Pt and Rh.[95,96] All geometry optimizations were performed in C_1 symmetry with subsequent vibrational frequency analysis to confirm that each stationary point was a minimum on the potential energy surface. Orbitals were visualized using *Molekel* 4.3.win32.[97]

The percentage of platinum, rhodium, or halide character in the occupied (canonical) molecular orbitals (MOs) and virtual orbitals

dx.doi.org/10.1021/ic300004x | *Inorg. Chem.* 2012, 51, 5152−5163

Scheme 3

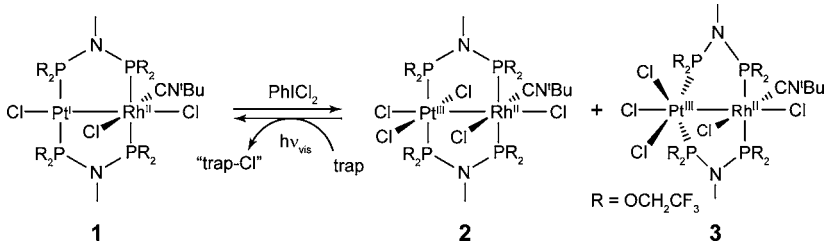

discussed for complexes **2** and **3** were calculated from a full population analysis, using eq 1,

$$\%\text{Orbital Character}_{(\text{Pt,Rh or Cl})} = \frac{\sum \phi^2_{(\text{Pt,Rh or Cl})}}{\sum \phi^2_{(\text{all})}} \times 100\% \quad (1)$$

where $\sum \phi_i$ (i = Pt, Rh, Cl, or all) is the sum of the squares of the eigenvalues associated with the atomic orbital (AO) of interest and all of the AOs in a particular MO, respectively. The vertical singlet transition energies of the complexes were computed at the time-dependent density functional theory (TD-DFT) level within G03 using the ground-state optimized structure.

RESULTS

Synthesis and Characterization. Heterobimetallic $Pt^{I}Rh^{II}$ complexes are furnished by sequential addition of tfepma, CN^tBu, and $Pt(cod)X_2$ to $\{Rh(cod)X_2\}_2$. Formation of a heterobimetallic compound by treatment of a metal–phosphine complex with a second metal source is a strategy that was pioneered by Shaw[98,99] and is a method that appears general for the assembly of heterobimetallic species.[66,100] Delivery of Cl_2 to PtRh(tfepma)$_2$(CN^tBu)Cl_3 (**1**) via $PhICl_2$ results in clean oxidative addition to produce *trans*-PtRh(tfepma)$_2$(CN^tBu)Cl_5 (**2**), which can be converted to *cis*-PtRh(tfepma)$_2$(CN^tBu)Cl_5 (**3**) via recrystallization in pentane (Scheme 3). The $^{31}P\{^1H\}$ NMR spectra for **1**–**3** are diagnostic of an idealized C_s symmetric heterobimetallic structure possessing two resonances corresponding to the Pt-bound and Rh-bound phosphorus atoms. The Pt-bound phosphorus atoms are easily identified by the presence of platinum satellites. The Pt–P coupling is on the order of ~4300 Hz in **1** and **3**, while the coupling in **2** is reduced to ~3000 Hz. The Rh-bound phosphorus chemical shifts are affected marginally by the oxidation of the metal core (by ~12 ppm from 112.6 ppm (**1**) to 101.0 ppm in **2** and to 103.8 ppm in **3**). In contrast, the Pt-bound phosphorus resonance shifts considerably upfield from 123.15 ppm in **1** to 64.45 in **2** and to 46.5 ppm in **3**. This is consistent with the accommodation of two chloride ligands at Pt upon oxidation as opposed to the Rh environment, which is relatively unaltered. Only minor changes in the chemical shift of the ^1H signals are observed upon oxidation. Similar to the oxidation of **1**, treatment of PtRh(tfepma)$_2$(CN^tBu)Br_3 (**4**) with Br_2 results in a quantitative formation of PtRh(tfepma)$_2$(CN^tBu)Br_5 (**5**; Scheme 4). As revealed by its X-ray crystal structure (vide infra), **5** possesses a meridional bromide configuration and a *trans* phosphine arrangement, analogous to the structure of **2**. The two phosphorus resonances observed at 111.7 ($^1J_{Pt-P}$ = 7147.5 Hz) and 110.1 ppm in the $^{31}P\{^1H\}$ NMR spectrum of **4** shift to 47.9 ($^1J_{Pt-P}$ = 4829.2 Hz) and 71.7 ppm and correspond to the Pt-bound and Rh-bound phosphorus atoms, respectively.

Scheme 4

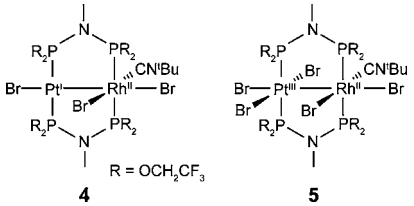

X-ray crystal structures obtained for the chloride suite of the PtRh heterobimetallic complexes are shown in Figure 1, and the crystallographic summary is given in Table 1. The structure of **1** is characterized by a square planar environment about the Pt center and an octahedral environment about the Rh center. Nearly linear bond angles of 175.20(3)° and 174.42(4)° are observed for P–Pt–P and Cl–Pt–Rh, respectively. The octahedral coordination of Rh is slightly more distorted, with the equatorial chloride and CN^tBu ligands bent toward the Pt center, giving a Cl–Rh–C bond angle of 162.03(11). The P–N distances of the tfepma backbone are effectively symmetric with a Δd_{P-N}(avg) of 0.0045 Å. The metal–chloride and metal–phosphorus bond distances of **1**–**3** are within the standard ranges for complexes of these types.

The structure of **2** shows that net addition of Cl_2 occurs at the Pt center of **1** to give octahedral coordination environments about both Pt and Rh. The equatorial Cl and CN^tBu ligands no longer bend toward the opposite metal center as in **1**; they instead bow slightly away from the Pt, as indicated by C(1)–Rh(1)–Pt(1) and Cl(4)–Rh(1)–Pt(1) angles of 91.15(9)° and 93.88(2)°, respectively. The Pt–Rh distance increases slightly from 2.6360(3) Å in **1** to 2.7053(3) Å in **2**. While the metal–phosphorus bonds are eclipsed in **1**, the metal core twists upon oxidation to result in a P(1)–Pt(1)–Rh(1)–P(2) torsion of 25.28°.

The Pt–Rh distance of **3** is almost identical to that of **2** at 2.7052(5) Å. The most notable structural difference between the two isomers is the location of the Pt-bound chlorides; **3** assumes a facial chloride arrangement, whereas **2** features a meridional chloride arrangement. The equatorial chloride ligands in **3** are compressed slightly relative to the phosphorus atoms with Cl(1)–Pt(1)–Cl(2) and P(1)–Pt(1)–P(3) angles of 89.75(4)° and 103.23(4)°, respectively. Asymmetric P–N bonding of the tfepma bridging ligands is slightly more pronounced in the oxidized complexes with a Δd_{P-N}(avg) of 0.025 and 0.018 Å for **2** and **3**, respectively; the P–N bonds on the Pt side of the molecules are shorter.

The structures of **4** and **5** are similar to those of their chloride counterparts, **1** and **2**. The X-ray crystal structures are shown in Figures S1 and S2 and crystallographic summaries are presented in Tables S1 and S2. **4** has a square planar Pt environment and an octahedral Rh environment with a metal–metal separation of 2.6503(7) Å. As in the structure of **1**, the CN^tBu and equatorial

dx.doi.org/10.1021/ic300004x | Inorg. Chem. 2012, 51, 5152–5163

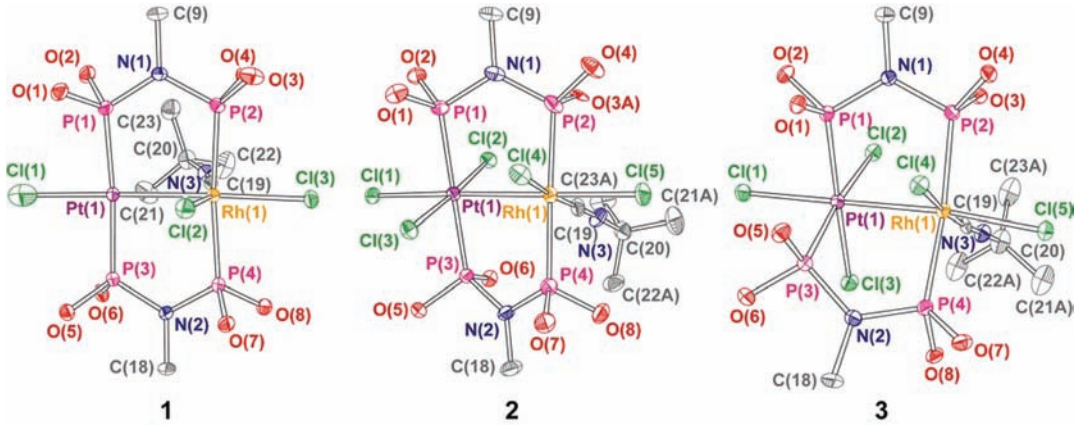

Figure 1. Thermal ellipsoid plots of **1**−**3** shown at the 50% probability level. Hydrogen atoms, (CH_2CF_3) groups of the tfepma bridging ligands, and solvents of crystallization have been omitted for clarity. For **2** and **3** only one part of the positional disorder has been shown.

Table 1. Crystal Data and Structure Refinement Statistics for 1−3

	1	2·0.5CH_2Cl_2	3
formula	$C_{23}H_{31}Cl_3F_{24}N_3O_8P_4PtRh$	$C_{23.50}H_{31}Cl_6F_{24}N_3O_8P_4PtRh$	$C_{23}H_{31}Cl_5F_{24}N_3O_8P_4PtRh$
fw	1461.74	1574.09	1532.64
temperature, K	100(2)	100(2)	100(2)
cryst. syst.	monoclinic	monoclinic	monoclinic
space group	$P2_1/n$	$P2/c$	$P2_1/c$
color	yellow	orange	orange
a (Å)	13.3954(10)	18.5258(15)	18.965(3)
b (Å)	19.3358(15)	11.3342(9)	10.4119(14)
c (Å)	17.9128(14)	24.5896(19)	25.015(3)
α (deg)	90	90	90
β (deg)	95.5030(10)	108.0650(10)	103.077(4)
γ (deg)	90	90	90
volume (Å^3)	4618.2(6)	4908.7(7)	4811.5(11)
Z	4	4	4
GOF[a]	1.028	1.062	1.016
R1 (all data)[b]	0.0429	0.0378	0.0670
wR2 (all data)[c]	0.0780	0.0726	0.0808
R1[b] [$(I > 2\sigma)$]	0.0327	0.0300	0.0385
wR2[c] [$(I > 2\sigma)$]	0.0727	0.0683	0.0707

[a] GOF = $[\Sigma w(F_o^2 - F_c^2)^2/(n-p)]^{1/2}$ where n is the number of data and p is the number of parameters refined. [b] R1 = $\Sigma||F_o| - |F_c||/\Sigma|F_o|$. [c] wR2 = $[\Sigma(w(F_o^2 - F_c^2)^2)/\Sigma(w(F_o^2)^2)]^{1/2}$.

bromide ligand of **4** are bent, giving a C−Rh−Br angle of 159.9(2)°. The crystal structure of **5** reveals the longest metal−metal separation of the complexes discussed here as a distance of 2.7408(1) Å was found between the octahedral Pt and octahedral Rh metal centers. The metrics and thermal ellipsoid plots for **4** and **5** are detailed in Tables S1 and S2 and Figures S1 and S2.

Photochemistry. The electronic absorption spectra of **1**−**3** are shown in Figure 2, and the spectra of **4** and **5** are shown in Figure 3. The spectrum of **1** is dominated by an intense band at 281 nm (ε = 24,800 M^{-1} cm^{-1}) that is flanked by a much weaker band at 372 nm (ε = 3600 M^{-1} cm^{-1}) and a slight shoulder at 433 nm (ε = 800 M^{-1} cm^{-1}). Oxidation of **1** results in a bathochromic shift of the highest intensity absorption feature of both **2** and **3**. Although λ_{max} is similar for the two isomers, the extinction coefficient of **2** is higher (ε = 21,300 in M^{-1} cm^{-1} in **2**, ε = 14,900 M^{-1} cm^{-1} in **3**). In addition, a pronounced absorption at 468 nm (ε = 4300 M^{-1} cm^{-1}) for **3**

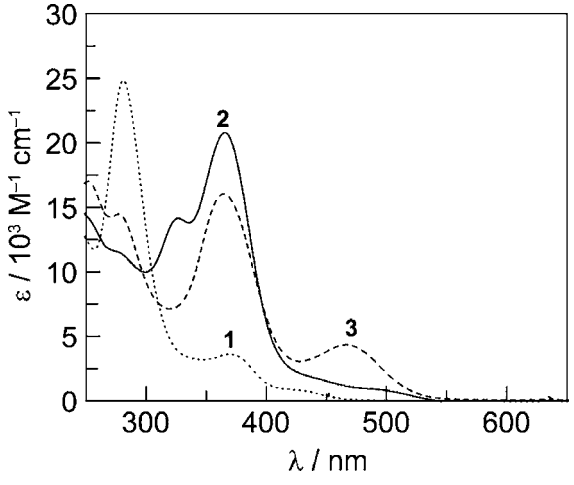

Figure 2. Extinction spectra of **1** (dotted, ●●●), **2** (dashed, − − −), and **3** (solid, —) in CH_3CN at 25 °C.

dx.doi.org/10.1021/ic300004x | Inorg. Chem. 2012, 51, 5152−5163

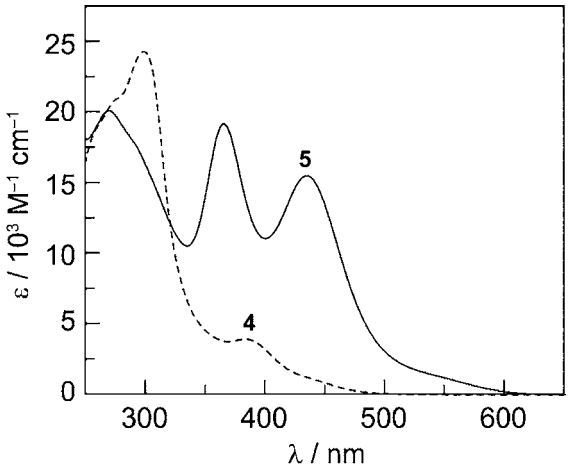

Figure 3. Extinction spectra of **4** (dashed,– – –) and **5** (solid, —) in CH_3CN at 25 °C.

is notably absent in **2**. The profiles of **1** and **4** are similar, but the latter is red-shifted. This red-shift is even more pronounced when comparing the spectra of **5** to **2**. Whereas the oxidized chloride complex has an absorption band that tails into the visible spectral region, the bromide complex contains a distinct peak at λ_{max} = 445 nm.

Irradiation of **2** in the presence of either 1-hexene or DMBD cleanly yields **1** (Figure 4). The persistence of a single isosbestic

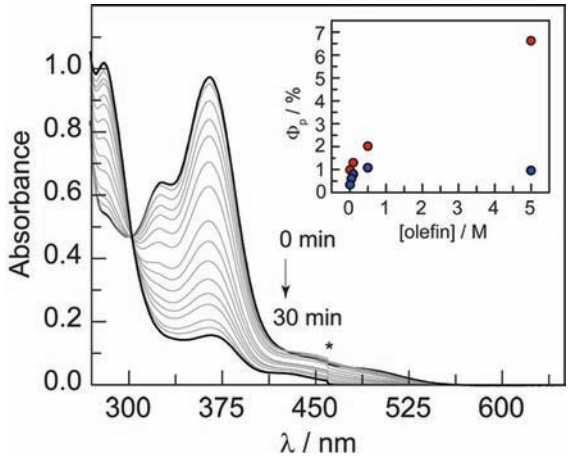

Figure 4. Photolysis of a 52 μM solution of **2** in CH_3CN with 0.1 M DMBD irradiated at 410 nm at 25 °C. Inset shows the quantum yield dependence (λ_{exc} = 410 nm) on olefin concentration for DMBD (●, red circles) and 1-hexene (●, blue circles).

point at ~300 nm attests to a pristine photoreaction as does the $^{31}P\{^1H\}$ NMR spectra of photolyzed solutions of **2** (Figure S3). Once conversion to **1** is achieved, continued irradiation leads to no further reaction, and no noticeable decomposition products are observed in the $^{31}P\{^1H\}$ NMR spectrum. The isosbestic point is only maintained under air-free photolysis conditions; in the presence of oxygen, **1** is still formed; however, the reaction is not quantitative. As Figure S5 indicates, the reaction proceeds similarly in the absence of olefin, and an isosbestic point is maintained. However, it should be noted that the final absorbance based on the measured molar absorptivity coefficients indicates that the conversion is not complete (yield ~87%). Since an isosbestic point is maintained, a small fraction (<13%) must photolyze to a product that does not absorb significantly in the observed spectral window. The byproduct is formed in an amount below the detection limits of $^{31}P\{^1H\}$ NMR; the only product observed is **1**.

Photolysis of **3** with visible light (λ_{exc} = 436 nm) produces **1** cleanly, even in the absence of olefin, as monitored by the $^{31}P\{^1H\}$ NMR spectrum of the photoproduct (Figure S4). The UV–vis photolysis traces shown in Figure 5 maintain an isosbestic

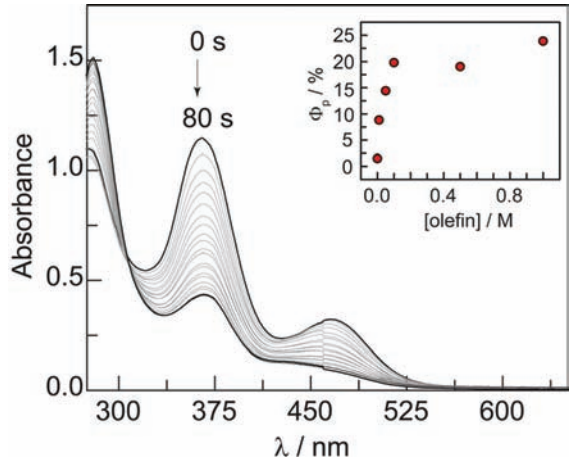

Figure 5. Photolysis of a 76 μM solution of **3** in CH_3CN irradiated at 434 nm at 25 °C with no olefin present. Inset shows the quantum yield dependence (λ_{exc} = 434 nm) on DMBD concentration (●, red circles).

point at 325 nm throughout the conversion for **3** in the presence of olefin or in the absence of trap. As shown in the insets of Figures 4 and 5 for **2** and **3**, respectively, the efficiency of halogen photoelimination depends on the concentration of the trap. The highest measured quantum yield for **2** was 6.6% in the presence of 5 M DMBD, whereas **3** proved more efficient, achieving a quantum efficiency of 23.4% in the presence of 1 M DMBD. The photochemistry of **3** also exhibits an air-sensitivity that is similar to that observed for **2**.

Solutions of **5** in THF with no DMBD were found to be stable in ambient light at room temperature. Upon irradiation with 434 nm light, spectral changes consistent with conversion of **5** to **4** were observed (Figure 6). The conversion of **5** to **4** in trap-free THF proceeds with a quantum yield of 7%.

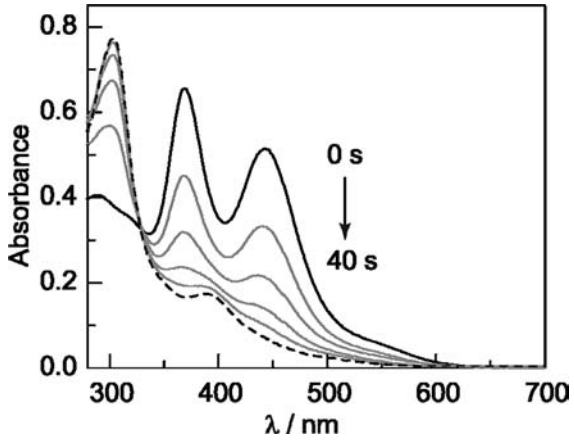

Figure 6. Photolysis of a 34 μM solution of **5** in THF irradiated at 434 nm at 25 °C. A quantum yield of 7.0% was calculated for this photoreaction.

dx.doi.org/10.1021/ic300004x | Inorg. Chem. 2012, 51, 5152–5163

In the presence of DMBD, **5** is observed to thermally react to **4**, thus obviating trap-dependence photochemical studies. **5** cleanly reduces to **4** in the presence of DMBD during a period of 2 h, as monitored by UV−vis spectroscopy (Figure 7).

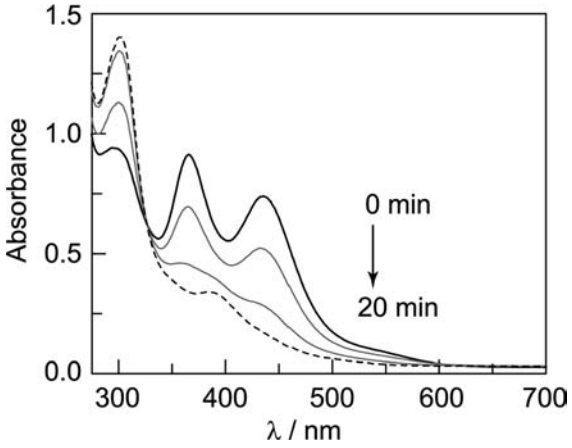

Figure 7. Spectral evolution of the absorption of a CH_3CN solution of **5** with 0.1 M DMBD present, indicating thermal conversion to **4** at 25 °C.

$^{31}P\{^1H\}$ NMR was used to monitor the reduction kinetics under pseudo-first-order conditions of DMBD ([DMBD] = 0.1−0.9 M; Figure S6). Rate constants were determined from plots of integration values for the sum of the two ^{31}P NMR resonances of **5** and the single ^{31}P NMR resonance of **4**, relative to the internal integration standard. Summed integration values for the disappearance of **5** and the appearance of **4** were fit with,

$$[PtRhBr_n] = [PtRhBr_n]_o + a\ \exp(-kt) \quad (2)$$

to furnish the pseudo-first-order rate constants listed in Table 2 for a concentration range of DMBD from 0.1 to 0.9 M.

Table 2. Summary of rate constants for the [DMBD] dependence of the thermal reduction of 5 to 4 as calculated from $^{31}P\{^1H\}$ integration values

[DMBD]/ M^{-1}	k ($PtRhBr_5$)/ $10^4\ s^{-1}$	k ($PtRhBr_3$)/ $10^4\ s^{-1}$	K (avg)/ $10^4\ s^{-1}$
0.1	4.13	3.61	3.87
0.3	4.42	4.67	4.54
0.5	4.12	3.58	3.85
0.7	3.60	3.12	3.36
0.9	3.25	3.38	3.31

The small amount of initial **4** arose from the thermal reaction occurring in the time between adding DMBD and inserting the sample into the spectrometer. Rate constants were on the order of $10^{-4}\ s^{-1}$, and no trap dependence was observed over DMBD concentrations used in the study.

Calculations. Ground-state density functional theory (DFT) calculations and time-dependent DFT (TDDFT) analysis were performed on models of **2** and **3**. To simplify the calculation, the OCH_2CF_3 groups of the tfepma bridging ligands were truncated to fluorine atoms (**2**-*f* and **3**-*f*). The frontier orbitals of **2**-*f* and **3**-*f* are distinct from the energy ordering of the classical metal−metal d(σ,π,δ) manifold[101] owing to the asymmetry of the PtRh ligand field. The orbital manifolds and isodensity plots of orbitals calculated for the electronic transitions of the two isomers are shown in Figure 8. For **2**-*f*, the metal orbitals of dπ symmetry are highly localized on the metal centers, and they are used to form chloride−metal pπ−dπ* antibonding orbitals (HOMO−7 and HOMO−6). The HOMO is a dσ orbital, usually found below the dπ and dδ orbitals. However, the additional antibonding contribution from the axial and equatorial chloride causes the orbital to become energetically destabilized. The LUMO possesses dσ* metal character as well as σ* character with the axial halides and Pt equatorial halides. The LUMO+1 and LUMO+2 are complementary σ* orbitals between the metal and equatorial ligands of Pt and Rh, respectively.

The electronic structure of **3**-*f* shares similar features to that of **2**-*f*. The HOMO−3 and HOMO−2 orbitals have metal−chloride π* character localized on Rh and Pt, respectively. The HOMO of **3**-*f* is also a dσ orbital similarly raised in energy due to chloride antibonding contributions. The LUMO is the complementary dσ* orbital, and it is antibonding with respect to the axial halides. The LUMO+1 is localized on Pt and possesses metal−chloride σ* character with the equatorial halides.

The primary contributions to the occupied orbitals come from the chloride ligands. The highest contribution of chloride character is in the HOMO−2 of **3**-*f* (90%). This trend inverts in the unfilled orbitals, with the chloride contribution dropping as low as 10% as seen in the LUMO+2 of **2**-*f*. The TDDFT analysis indicates that the lowest energy transitions of **2**-*f* arise from electron promotion from the HOMO, HOMO−6, and HOMO−7 to the LUMO, LUMO+1, and LUMO+2. For **3**-*f* the lowest energy transitions involve electron promotion from HOMO, HOMO−2, HOMO−3, HOMO−10, and HOMO−11 to LUMO and LUMO+1. (See Table S5 for TD-DFT results for **2** and Table S6 for TD-DFT results for **3**.) A plot showing the energies of the calculated excited states overlaid with the absorption spectra of **2** and **3** is shown in Figure S7.

Transient Spectroscopy. The high quantum yield for the photoconversion of **3** to **1** allowed for the interrogation of the X_2 photoelimination reaction by transient kinetics techniques. The air-sensitivity of the photoreaction required that solutions be prepared in a glovebox. In addition, the irreversibility of the conversion demanded that the samples were flowed and not recirculated. The transient absorption (TA) spectrum of **3** in the presence of 0.1 M DMBD displays a ground-state bleach within the 8 ns pulse width of the laser pump (Figure 9, solid red line). Superimposed on the ground-state bleach are pronounced absorptions centered at 375 and 320 nm. The observed TA spectrum does not match the computed difference spectrum of **1** and **3** (Figure 9, dotted line), indicating the presence of a unique intermediate. The absorption spectrum of the intermediate species shown in Figure 10 was obtained by adding the spectrum of **3** to the observed TA spectrum. The spectral features of the photointermediate show an intense absorption at 375 nm akin to the intense ground-state absorption feature of **3** and distinct absorptions at 330 and 430 nm.

In order to determine the fate of the intermediate, single wavelength kinetic traces were gathered at several wavelengths for a sample of **3** prepared in the presence of 0.2 M DMBD. This trap concentration was used because the trap-dependent quantum yield (Figure 5) does not appreciably increase above a DMBD concentration of 0.1 M. Thus, the TA signal is maximized for solutions containing more than 0.1 M DMBD. Figure 11 shows the single wavelength kinetic traces monitored at wavelengths about the isosbestic point between the photoreactant **3** and photoproduct **1**: to higher energy than

dx.doi.org/10.1021/ic300004x | Inorg. Chem. 2012, 51, 5152−5163

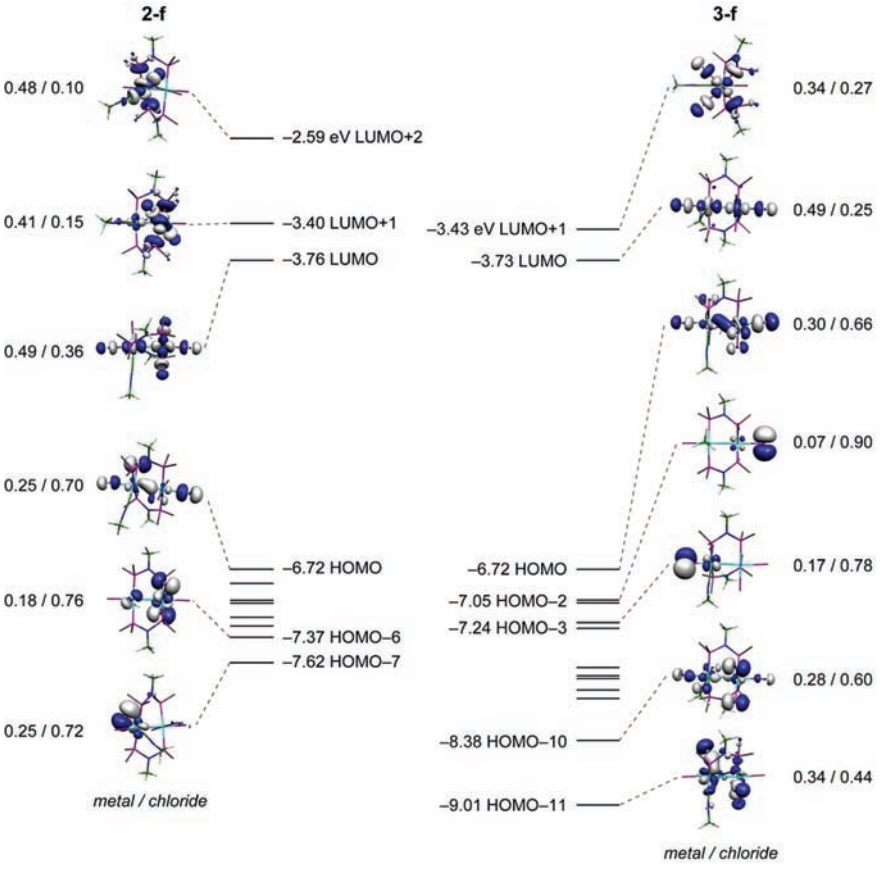

Figure 8. Molecular orbital diagram of **2**-*f* (left) and **3**-*f* (right). Isodensity plots (isovalue = 0.5) are shown for the orbitals used in the transitions comprising the lowest energy excited states of the two isomers. The fractional numbers under the isodensity plots indicate the contribution of metal−chloride to each pictured orbital.

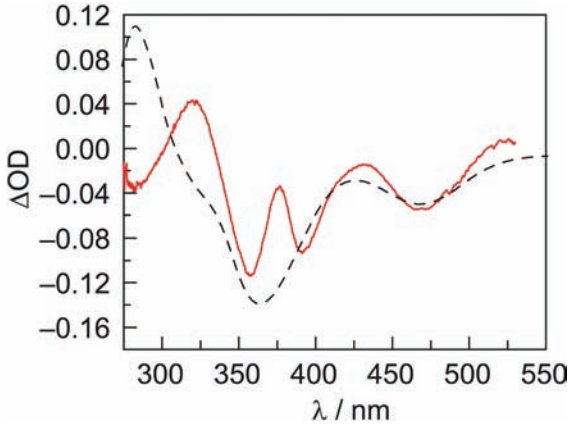

Figure 9. Transient absorption spectrum of **3** in CH_3CN and 0.1 M DMBD at 0 ns delay time with a 355 nm pump wavelength and a broadband probe (solid red, —). The normalized difference spectrum of **1** and **3** is also shown (dashed, – – –).

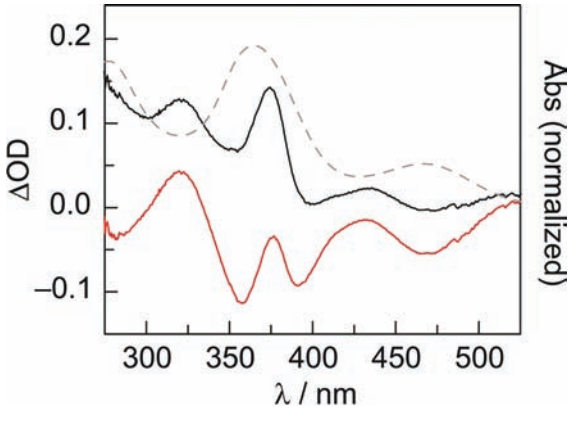

Figure 10. Absorption spectrum of **3** (dashed gray, – – –) and transient absorption spectrum of **3** in CH_3CN and 0.1 M DMBD at 0 ns delay time with a 355 nm pump wavelength and a broadband probe (solid red, —). Adding a normalized spectrum of **3** to the 0 ns TA spectrum generates an absorption spectrum of the photointermediate (solid black, – – –).

the isosbestic point (320 nm), at the isosbestic point (325 nm), and to lower energy than the isosbestic point (327 nm). Because the ground-state absorption of **1** is greater than that of **3** at all wavelengths blue of the isosbestic point, a single wavelength trace that decays to a positive ΔOD supports that the conversion of **3** to **1** has occurred. Likewise, a decay to a ΔOD of zero at the isosbestic point (325 nm) is expected and observed for the conversion of **3** to **1**. The ΔOD is not zero at this wavelength because of the presence of the photointermediate. At wavelengths lower in energy than the isosbestic point, **3** absorbs more than **1**. Thus, the single wavelength trace at 327 nm shows a decay to a negative ΔOD at longer times. All three traces were invariant beyond the 200 μs window shown in Figure 11.

Figure 12 shows single wavelength traces monitored about the isosbestic point at 337 nm for the photointermediate **3** and the photoproduct **1**. Because the photointermediate is formed within the 8 ns pulse-width of the laser, the ΔOD should be

dx.doi.org/10.1021/ic300004x | *Inorg. Chem.* 2012, 51, 5152−5163

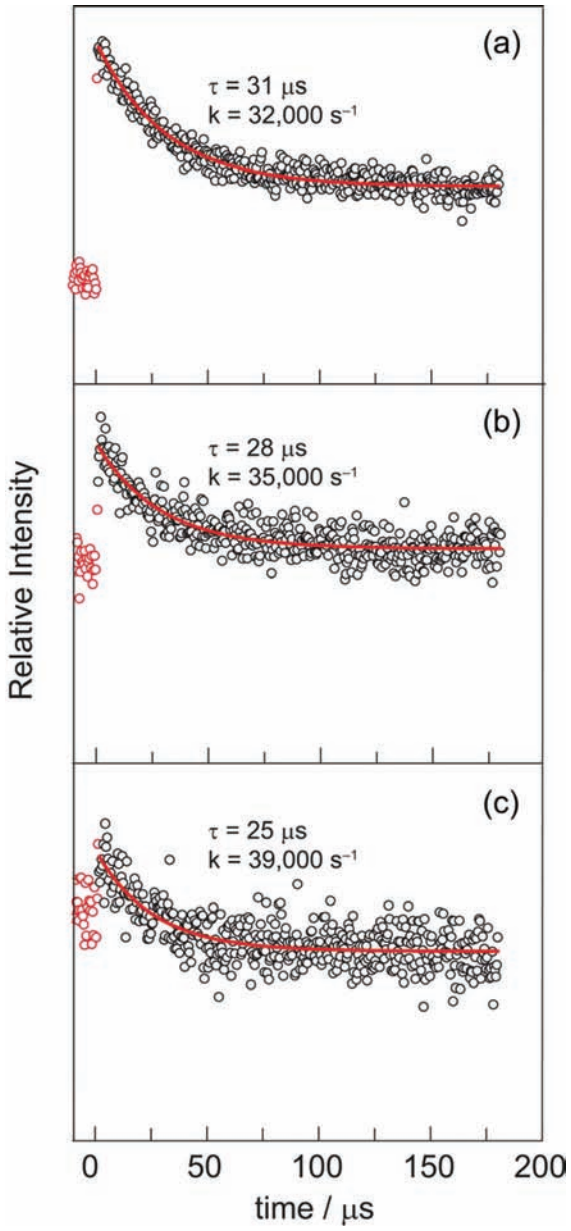

Figure 11. Single wavelength kinetic traces of CH_3CN solutions of **3** pumped at 355 nm and monitored at (a) 320 nm, (b) 325 nm, and (c) 327 nm.

invariant at all time points, as is observed in Figure 12. This result supports that a single, fully formed intermediate smoothly converts directly to the photoproduct, and that the photointermediate is the only existent species prior to halogen reductive elimination. The ΔOD exhibits as a negative value at the isosbestic point because both the photointermediate and **1** absorb less than **3** at 337 nm. At 390 nm, the ΔOD is observed to recover from an initially negative ΔOD, ultimately leveling out at a negative ΔOD at longer time points owing to the greater absorption of **3** relative to that of **1**.

Because the photointermediate is produced in the lifetime of the laser pulse, and converts directly to photoproduct **1**, single wavelength kinetics at all wavelengths should report only on the lifetime of the photointermediate. The lifetimes determined for the decay traces at a variety of wavelengths are summarized in Table 3. The average lifetime of the photointermediate is 27 μs ($k = 3.6 \times 10^4$ s^{-1}).

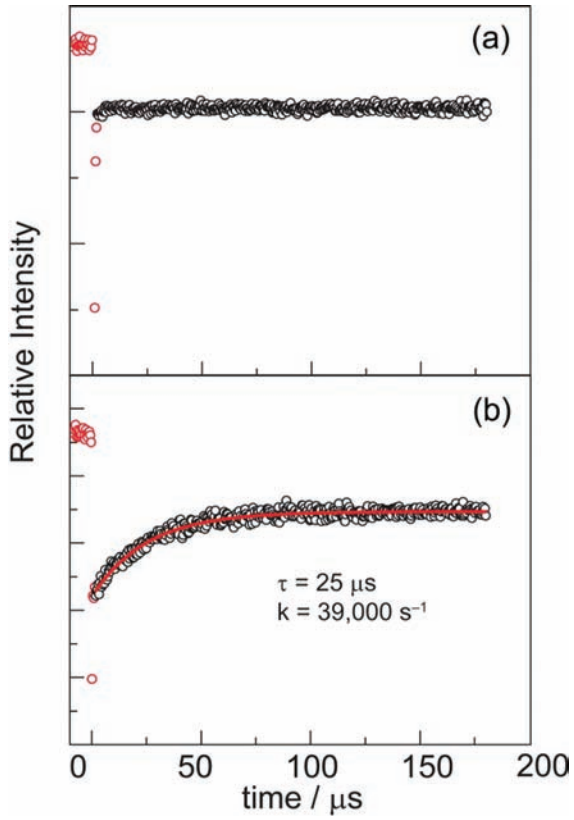

Figure 12. Single wavelength kinetic traces of CH_3CN solutions of **3** pumped at 355 nm recorded at (a) 337 nm and (b) 390 nm.

Table 3. Lifetimes Determined from Single-Wavelength Transient Absorption Traces for CH_3CN Solutions of 3 Pumped at 355 nm in the Presence of 0.2 M DMBD

λ/nm	τ/μs	k/s^{-1}
320	31	32,000
325	28	35,000
327	25	39,000
337	25	39,000
–	27 ± 3[a]	36,000

[a]Average value of all entries.

A trap-dependence study was undertaken on samples of **3** to determine if the decay of the intermediate was sensitive to olefin. Experiments were performed at four DMBD concentrations at which the quantum yield for the conversion of **3** to **1** was not expected to change (see Figure 5): 0.1, 0.2, 0.4, and 0.6 M. Data were also collected at DMBD concentrations below 0.1 M, at which the quantum yield was sensitive to trap: 0.05, 0.01, 0.005, and 0.001 M. The lifetimes of the intermediate at these concentrations are summarized in Table 4. No significant change in the lifetime of the intermediate (τ_{avg} = 31 μs) was observed regardless of the amount of DMBD present, including a sample prepared with only CH_3CN (no DMBD).

DISCUSSION

Compounds **1** and **4** expand the library of $Pt^{I}Rh^{II}$ complexes that possess the 3:5 structure type. They are prepared from the first rational, high-yielding syntheses of this compound type, and join $Pt^{I}Rh^{II}(Ph_2AsCH_2PPh_2)(CO)X_3$ as the only neutral 3:5 halide complexes. The Pt−Rh distance of 2.6360(3) Å in **1**

dx.doi.org/10.1021/ic300004x | Inorg. Chem. 2012, 51, 5152−5163

Table 4. Lifetimes Determined from Single-Wavelength Transient Absorption Traces at Various DMBD Concentrations

[DMBD]/M	λ/nm	τ/μs	k/s^{-1}
0.6	325	30	34,000
0.4	325	31	32,000
0.2	325	28	35,000
0.1	325	30	34,000
0.05	325	31	32,000
0.01	325	34	29,000
0.005	325	33	30,000
0.001	325	31	32,000
–	–	31 ± 1.7[a]	32,000

[a]Average value of all entries.

is consistent with the single metal−metal bonds (2.59−2.74 Å) of other 3:5 heterobimetallic complexes. The metal−metal bond of **1** follows from the pairing of the odd electrons residing in the dσ orbitals of d^9 and d^7 centers. The electronic absorption spectrum of **1** is dominated by a tailing absorption into the visible region that is ascribed to halide-to-metal charge transfer. This is consistent with the spectral assignment of the related 3:5 complex, $[PtRh(dppm)_2(MeNC)_3Cl](PF_6)_2$, which also exhibits a tailing LMCT absorption feature.[69] The stabilization of the 3:5 structure does not appear to rely on the electronic asymmetry of the P−N—P backbone since the Δd_{P-N}(avg) of only 0.0045 Å is an order of magnitude smaller than that observed for $Rh_2^{0,II}(tfepma)_3Cl_2$.

Halogen photoelimination from **2**, **3**, and **5** is consistent with the newly discovered proclivity of late heterobimetallic complexes to promote M−X bond activation.[53,58,59,102] Halogen elimination from **5** proceeds thermally in the presence of an olefin trap. The pseudo-first-order rate constant for the thermal reduction of **5** to **4** shows no olefin trap dependence as measured by $^{31}P\{^1H\}$ NMR. This result suggests that Br_2 trapping by olefin is not rate limiting. Two potential reaction paths consistent with this observation are a rate-limiting (i) dissociation of weakly bound Br_2 or (ii) elimination of Br radical, which then undergoes a thermal reaction with olefin. The direct bimolecular reaction between the oxidized metal complex and olefin is ruled out by these results. In contrast, halogen elimination from **2** and **3** must be promoted photochemically. The stability of **2** and **3** to thermal reduction of Cl_2 in the presence of the olefin trap can likely be attributed to stronger Pt−Cl bonds and a higher barrier to thermal dissociation.

The photoreaction of **3** is distinguished by its exceptionally high quantum yield as compared to those of **2** and other homo- and heterobimetallic complexes. In **3**, *cis* equatorial chlorides may eliminate directly from the Pt center, whereas in **2** the *trans* arrangement of the equatorial chlorides prevents such an elimination. In these cases, we speculate that elimination typically requires rearrangement of the departing ligand into a bridging position. Such bridged intermediates have been proposed for both the reductive elimination of H_2 from bimetallic cores and in the photochemistry of bimetallic metal-halide complexes.[46,103]

The calculations performed on **2**-*f* and **3**-*f* support the contention that M−X bond photoactivation is driven by LMCT excitation.[58] The results of TDDFT suggest that the lowest energy absorption may best be described as chloride-based LMCT. Parent orbitals involved in the lowest energy excited states of **2**-*f* and **3**-*f* comprise occupied orbitals of predominantly halide character and metal-based virtual orbitals. In addition, the virtual orbitals are strongly σ antibonding in character; population of these orbitals serves to disrupt the M−X bonding, not only for the axial halides but as shown in orbitals **2**-155, **2**-156, and **3**-154, the equatorial halides as well.

The high quantum yield for the photoconversion of **3** to **1** suggests that primary photoproducts may be generated at significant concentrations. Thus, **3** permits the photochemical transformation relevant to reductive elimination of halogen from the metal complex to be observed directly by transient kinetic methods. Since the photochemistry of **3** is quantitative in the presence of trap, all observed processes must account for the regeneration of the ground state of **3** and productive formation of **1**.

The zero-delay TA spectrum shown in Figure 9 indicates that the ground-state spectrum of **3** is fully bleached within the pulse-width of the 8 ns laser pump. The observation of a nonzero ΔOD at time zero monitored at the isosbestic point in the conversion of **3** to **1** (see Figure 11) indicates that the reaction is not completed during the laser pulse-width and an intermediate is present. This result is further supported by the mismatch between the zero-delay TA spectrum and the calculated difference spectrum of **3** and **1** (Figure 9). If the conversion of **3** to **1** occurred during the 8 ns pulse-width, the zero-delay TA spectrum would simply match the difference spectrum of **3** and **1**, which is not the case. Thus, a discrete intermediate forms as a photoproduct within the first 8 ns after absorption of a photon. This intermediate converts to **1** with a 31 μs lifetime regardless of the concentration of DMBD present. Furthermore, the isosbestic point observed at 337 nm (Figure 12) in the conversion of intermediate to **1** suggests that **1** is the sole product after intermediate formation.

The qualitative absorption spectrum of this long-lived photointermediate can be determined by adding the spectrum of **3** to the TA spectrum (see Figure 10). Since the spectrum of this photointermediate possesses features very similar to the ground-state spectrum of **3**, it must share a similar structure. As such, the photointermediate likely retains halogen. We have observed that elimination from two-electron mixed valence cores is facilitated by folding one of the eliminating atoms into the edge-bridging position.[73] In this case, the ligand-to-metal charge transfer transitions are retained, and the spectral profile would be expected to be similar to that of **3**, but is shifted as observed.

In summary, a neutral 3:5 heterobimetallic complex with a $ClPt^{I}Rh^{II}Cl_2$ core is readily oxidized to a $Cl_3Pt^{III}Rh^{II}Cl_2$ core. The *mer* oxidation product isomerizes to the *fac* isomer when dissolved in pentane solution. Irradiation of either isomer induces halogen elimination to reform the $ClPt^{I}Rh^{II}Cl_2$ core. For concentrations of DMBD less than 0.1 M, the quantum yield for halogen elimination from *fac*-$Cl_3Pt^{III}Rh^{II}Cl_2$ complex exceeds that of $Pt_2(tfepma)_2Cl_6$, the most efficient complex for halogen elimination measured to date. The lowest energy excited states of the $Cl_3Pt^{III}Rh^{II}Cl_2$ core of **3** exhibit significant halide-to-metal charge transfer character, which appears to effectively promote the weakening and disruption of the M−X bonds. The exceptionally high quantum yield for the **3** → **1** photoelimination reaction permits the detection, for the first time, of an intermediate that precedes halogen reductive elimination. The photointermediate is generated promptly upon excitation (within 8 ns), and it eliminates halogen to produce **1** on a microsecond time scale. The calculated absorption spectrum of the intermediate is similar to **3**, suggesting that halogen has not been formally eliminated yet. Parallel to H_2 elimination reactions, reductive elimination may proceed by coupling a terminal halogen to one residing in a

dx.doi.org/10.1021/ic300004x | Inorg. Chem. 2012, 51, 5152−5163

Scheme 5

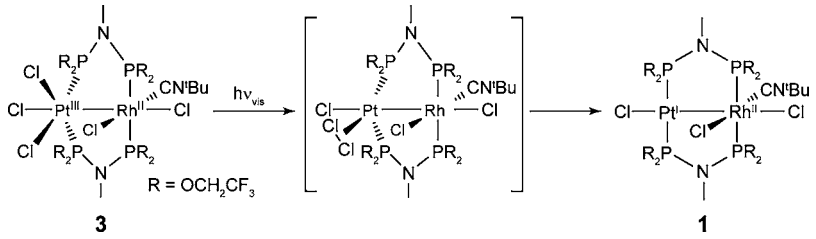

μ-bridging position across the metal−metal bond, or from coupling of two halides on a single metal site. In this case, the photointermediate is likely a Cl_2-adduct species (see Scheme 5), analogous to the H_2-adduct intermediates proposed in H_2 elimination.[76] This intermediate is expected to preserve the overall charge transfer absorption profile that is characteristic of **3** but simply shifted in energy. The transient absorption spectrum of the photointermediate is consistent with this contention. In this model, the decay of the photointermediate is thus a result of halogen elimination; the rate constant for this halogen reductive elimination is measured to be 3.2×10^4 s^{-1}. This rate constant provides the first metric for the rational design of a HX splitting cycle. As M−X photoactivation and elimination is the critical step in achieving energy storage via HX splitting, the ability to probe the kinetics of MX photoactivation directly will be invaluable to the rational design of photocatalysts that strike a balance in managing the formal reduction of protons to hydrogen but at the same time are oxidizing enough to efficiently eliminate halogen.

■ ASSOCIATED CONTENT

Supporting Information

TDDFT results, laser kinetic single wavelength traces, NMR-scale photolysis data, additional UV−vis photolysis plots, and crystallographic information files. This material is available free of charge via the Internet at http://pubs.acs.org

■ AUTHOR INFORMATION

Corresponding Author

*E-mail: nocera@mit.edu.

Notes

The authors declare no competing financial interest.

■ ACKNOWLEDGMENTS

This research was supported by the NSF (Grant CHE-1112154). Grants from the NSF also provided instrument support to the DCIF at MIT (CHE-9808061, DBI-9729592). B.D.M. was supported by the Paul E. Gray Fund and the MIT UROP program. D.A.L. thankfully acknowledges the Jane Coffin Childs Memorial Fund for Medicinal Research for a postdoctoral fellowship.

■ REFERENCES

(1) Nocera, D. G. *Inorg. Chem.* **2009**, *48*, 10001−10017.
(2) Lewis, N. S.; Nocera, D. G. *Proc. Natl. Acad. Sci. U.S.A.* **2006**, *103*, 15729−15735.
(3) Abbott, D. *Proc. IEEE* **2010**, *98*, 42−66.
(4) Cook, T. R.; Dogutan, D. K.; Reece, S. Y.; Surendranath, Y.; Teets, T. S.; Nocera, G. *Chem. Rev.* **2010**, *110*, 6474−502.
(5) Nocera, D. G. *Energy Environ. Sci.* **2010**, *3*, 993−5.
(6) Nocera, D. G. *ChemSusChem* **2009**, *2*, 387−390.
(7) Esswein, A. J.; Nocera, D. G. *Chem. Rev.* **2007**, *107*, 4022−4047.
(8) Kanan, M. W.; Nocera, D. G. *Science* **2008**, *321*, 1072−1075.
(9) Surendranath, Y.; Dinča, M.; Nocera, D. G. *J. Am. Chem. Soc.* **2009**, *131*, 2615−2620.
(10) McDaniel, N. D.; Coughlin, F. J.; Tinker, L. L.; Bernhard, S. *J. Am. Chem. Soc.* **2008**, *130*, 210−217.
(11) Schley, N. D.; Blakemore, J. D.; Subbaiyan, N. K.; Incarvito, C. D.; D'Souza, F.; Crabtree, R. H.; Brudvig, G. W. *J. Am. Chem. Soc.* **2011**, *133*, 10473−10481.
(12) Blakemore, J. D.; Schley, N. D.; Balcells, D.; Hull, J. F.; Olack, G. W.; Incarvito, C. D.; Eisenstein, O.; Brudvig, G. W.; Crabtree, R. H. *J. Am. Chem. Soc.* **2010**, *132*, 16017−16029.
(13) Hull, J. F.; Balcells, D.; Blakemore, J. D.; Incarvito, C. D.; Eisenstein, O.; Brudvig, G. W.; Crabtree, R. H. *J. Am. Chem. Soc.* **2009**, *131*, 8730−8731.
(14) Grotjahn, D. B.; Brown, D. B.; Martin, J. K.; Marelius, D. C.; Abadjian, M.-C.; Tran, H. N.; Kalyuzhny, G.; Vecchio, K. S.; Specht, Z. G.; Cortes-Llamas, S. A.; Miranda-Soto, V.; van Niekerk, C.; Moore, C. E.; Rheingold, A. L. *J. Am. Chem. Soc.* **2011**, *133*, 19024−19027.
(15) Gao, Y.; Akermark, T.; Liu, J. H.; Sun, L. C.; Akermark, B. *J. Am. Chem. Soc.* **2009**, *131*, 8726−8727.
(16) Dogutan, D. K.; McGuire, R. Jr.; Shao-Horn, Y.; Nocera, D. G. *J. Am. Chem. Soc.* **2011**, *133*, 9178−9180.
(17) Brimblecombe, R.; Swiegers, G. F.; Dismukes, G. C.; Spiccia, L. *Angew. Chem., Int. Ed.* **2008**, *47*, 7335−7338.
(18) Hocking, R. K.; Brimblecombe, R.; Chang, L.-Y.; Singh, A.; Cheah, M. H.; Glover, C.; Casey, W. H.; Spiccia, L. *Nature Chem.* **2011**, *3*, 461−466.
(19) Geletii, Y. V.; Botar, B.; Kögerler, P.; Hillesheim, D. A.; Musaev, D. G.; Hill, C. L. *Angew. Chem., Int. Ed.* **2008**, *47*, 3896−3899.
(20) Geletii, Y. V.; Besson, C.; Hou, Y.; Yin, Q.; Musaev, D. G.; Quiñonero, D.; Cao, R.; Hardcastle, K. I.; Proust, A.; Kögerler, P.; Hill, C. L. *J. Am. Chem. Soc.* **2009**, *131*, 17360−17370.
(21) Yin, Q.; Tan, J. M.; Besson, C.; Geletti, Y. V.; Musaev, D. G.; Kuznetsov, A. E.; Luo, Z.; Hardcastle, K. I.; Hill, C. L. *Science* **2010**, *328*, 342−345.
(22) Stracke, J. J.; Finke, R. G. *J. Am. Chem. Soc.* **2011**, *133*, 14872−14875.
(23) Chen, Z.; Concepcion, J. J.; Luo, H.; Hull, J. F.; Paul, A.; Meyer, T. J. *J. Am. Chem. Soc.* **2010**, *132*, 17670−17673.
(24) Concepcion, J. J.; Jurss, J. W.; Templeton, J. L.; Meyer, T. J. *J. Am. Chem. Soc.* **2008**, *130*, 16462−16463.
(25) Concepcion, J. J.; Jurss, J. W.; Norris, M. R.; Chen, Z.; Templeton, J. L.; Meyer, T. J. *Inorg. Chem.* **2010**, *49*, 1277−1279.
(26) Bernet, L.; Lalrempuia, R.; Ghattas, W.; Mueller-Bunz, H.; Vigara, L.; Llobet, A.; Albrecht, M. *Chem. Commun.* **2011**, *47*, 8058−8060.
(27) Romain, S.; Vigara, L.; Llobet, A. *Acc. Chem. Res.* **2009**, *42*, 1944−1953.
(28) Wasylenko, D. J.; Ganesamoorthy, C.; Henderson, M. A.; Koivisto, B. D.; Osthoff, H. D.; Berlinguette, C. P. *J. Am. Chem. Soc.* **2010**, *132*, 16094−16106.
(29) Wasylenko, D. J.; Ganesamoorthy, C.; Koivisto, B. D.; Henderson, M. A.; Berlinguette, C. P. *Inorg. Chem.* **2010**, *49*, 2202−2209.
(30) Symes, M. D.; Surendranath, Y.; Lutterman, D. A.; Nocera, D. G. *J. Am. Chem. Soc.* **2011**, *133*, 5174−5177.
(31) Kanan, M. W.; Yano, J.; Surendranath, Y.; Dincă, M.; Yachandra, V. K.; Nocera, D. G. *J. Am. Chem. Soc.* **2010**, *132*, 13692−13701.

(32) Esswein, A. S.; Surendranath, Y.; Reece, S. Y.; Nocera, D. G. *Energy Environ. Sci.* **2010**, *4*, 499−504.
(33) McAlpin, J. G.; Surendranath, Y.; Dincă, M.; Stitch, T. A.; Stoian, S.; Casey, W. H.; Nocera, D. G.; Britt, R. D. *J. Am. Chem. Soc.* **2010**, *132*, 6882−6883.
(34) McAlpin, J. G.; Stich, T. A.; Ohlin, C. A.; Surendranath, Y.; Nocera, D. G.; Casey, W. H.; Britt, R. D. *J. Am. Chem. Soc.* **2011**, *133*, 15444−15452.
(35) Surendranath, Y.; Kanan, M. W.; Nocera, D. G. *J. Am. Chem. Soc.* **2010**, *132*, 16501−16509.
(36) Kanan, M. W.; Surendranath, Y.; Nocera, D. G. *Chem. Soc. Rev.* **2009**, *38*, 109−114.
(37) Lutterman, D. A.; Surendranath, Y.; Nocera, D. G. *J. Am. Chem. Soc.* **2009**, *131*, 3838−3839.
(38) Wang, L.-P.; Wu, Q.; Van Voorhis, T. *Inorg. Chem.* **2010**, *49*, 4543−4553.
(39) Polyansky, D. E.; Muckerman, J. T.; Rochford, J.; Zong, R.; Thummel, R. P.; Fujita, E. *J. Am. Chem. Soc.* **2011**, *133*, 14649−14665.
(40) Concepcion, J. J.; Tsai, M.-K.; Muckerman, J. T.; Meyer, T. J. *J. Am. Chem. Soc.* **2010**, *132*, 1545−1557.
(41) Cape, J. L.; Siems, W. F.; Hurst, J. K. *Inorg. Chem.* **2009**, *48*, 8729−8735.
(42) Pijpers, J. J. H.; Winkler, M. T.; Surendranath, Y.; Buonassisi, T.; Nocera, D. G. *Proc. Natl. Acad. Sci. U.S.A.* **2011**, *108*, 10056−10061.
(43) Reece, S. Y.; Hamel, J. A.; Sung, K.; Jarvi, T. D.; Esswein, A. J.; Pijpers, J. J. H.; Nocera, D. G. *Science* **2011**, *334*, 645−648.
(44) Nocera, D. G. *Acc. Chem. Res.* **2012**, in press.
(45) Heyduk, A. F.; Nocera, D. G. *Science* **2001**, *293*, 1639−1641.
(46) Esswein, A. J.; Veige, A. S.; Nocera, D. G. *J. Am. Chem. Soc.* **2005**, *127*, 16641−16651.
(47) van Zyl, W. E.; López-de-Luzuriaga, J. M.; Fackler, J. P. Jr.; Staples, R. J. *Can. J. Chem.* **2001**, *79*, 896−903.
(48) Fackler, J. P. Jr. *Inorg. Chem.* **2002**, *41*, 6959−6972.
(49) Ovens, J. S.; Leznoff, D. B. *Dalton Trans.* **2011**, *40*, 4140−4146.
(50) Heyduk, A. F.; Macintosh, A. M.; Nocera, D. G. *J. Am. Chem. Soc.* **1999**, *121*, 5023−5032.
(51) Bellachioma, G.; Cardaci, G.; Macchioni, A.; Venturi, C.; Zuccaccia, C. *J. Organomet. Chem.* **2006**, *691*, 3881−3888.
(52) Odom, A. L.; Heyduk, A. F.; Nocera, D. G. *Inorg. Chim. Acta* **2000**, *297*, 330−337.
(53) Cook, T. R.; Esswein, A. J.; Nocera, D. G. *J. Am. Chem. Soc.* **2007**, *129*, 10094−10095.
(54) Lee, C. H.; Cook, T. R.; Nocera, D. G. *Inorg. Chem.* **2011**, *50*, 714−716.
(55) Teets, T. S.; Cook, T. R.; McCarthy, B. D.; Nocera, D. G. *Inorg. Chem.* **2011**, *50*, 5223−5233.
(56) Teets, T. S.; Cook, T. R.; McCarthy, B. D.; Nocera, D. G. *J. Am. Chem. Soc.* **2011**, *133*, 8114−8117.
(57) Teets, T. S.; Nocera, D. G. *J. Am. Chem. Soc.* **2011**, *133*, 17796−17806.
(58) Cook, T. R.; Surendranath, Y.; Nocera, D. G. *J. Am. Chem. Soc.* **2009**, *131*, 28−29.
(59) Teets, T. S.; Nocera, D. G. *J. Am. Chem. Soc.* **2009**, *131*, 7411−7420.
(60) Roundhill, D. M.; Gray, H. B.; Che, C.-M. *Acc. Chem. Res.* **1989**, *22*, 55−61.
(61) Cowie, M.; Dwight, S. K. *Inorg. Chem.* **1980**, *19*, 2500−2507.
(62) Hollis, L. S.; Lippard, S. J. *J. Am. Chem. Soc.* **1983**, *105*, 3494−3503.
(63) Barton, J. K.; Szalda, D. J.; Rabinowitz, H. N.; Waszczak, J. V.; Lippard, S. J. *J. Am. Chem. Soc.* **1979**, *101*, 1434−1441.
(64) Matsumoto, K.; Moriyama, H.; Suzuki, K. *Inorg. Chem.* **1990**, *29*, 2096−2100.
(65) Micklitz, W.; Riede, J.; Huber, B.; Mueller, G.; Lippert, B. *Inorg. Chem.* **1988**, *27*, 1979−1986.
(66) Hassan, F. S. M.; Markham, D. P.; Pringle, P. G.; Shaw, B. L. *J. Chem. Soc., Dalton Trans.* **1985**, 279−283.
(67) Hui, C.-K.; Chu, B. W.-K.; Zhu, N.; Yam, V. W.-W. *Inorg. Chem.* **2002**, *41*, 6178−6180.
(68) Pamplin, C. B.; Rettig, S. J.; Patrick, B. O.; James, B. R. *Inorg. Chem.* **2003**, *42*, 4117−4126.
(69) Balch, A. L.; Catalano, V. J. *Inorg. Chem.* **1992**, *31*, 3934−3942.
(70) Balch, A. L.; Guimerans, R. R.; Linehan, J.; Olmstead, M. M.; Oram, D. E. *Organometallics* **1985**, *4*, 1445−1451.
(71) Farr, J. P.; Olmstead, M. M.; Balch, A. L. *J. Am. Chem. Soc.* **1980**, *102*, 6654−6656.
(72) Heyduk, A. F.; Nocera, D. G. *Chem. Commun.* **1999**, 1519−1520.
(73) Gray, T. G.; Veige, A. S.; Nocera, D. G. *J. Am. Chem. Soc.* **2004**, *126*, 9760−9768.
(74) Gray, T. G.; Nocera, D. G. *Chem. Commun.* **2005**, 1540−1542.
(75) Veige, A. S.; Nocera, D. G. *Chem. Commun.* **2004**, 1958−1959.
(76) Veige, A. S.; Gray, T. G.; Nocera, D. G. *Inorg. Chem.* **2005**, *44*, 17−26.
(77) Heyduk, A. F.; Nocera, D. G. *J. Am. Chem. Soc.* **2000**, *122*, 9415−9426.
(78) Yip, H.-K.; Lin, H.-M.; Wang, Y.; Che, C.-M. *Inorg. Chem.* **1993**, *32*, 3402−3407.
(79) Xia, B.-H.; Zhang, H.-X.; Che, C.-M.; Leung, K.-H.; Phillips, D. L.; Zhu, N.; Zhou, Z.-Y. *J. Am. Chem. Soc.* **2003**, *125*, 10362−10374.
(80) Bailey, J. A.; Hill, M. G.; Marsh, R. E.; Miskowski, V. M.; Schaefer, W. P.; Gray, H. B. *Inorg. Chem.* **1995**, *34*, 4591−4599.
(81) Harvey, P. D.; Schaefer, W. P.; Gray, H. B. *Inorg. Chem.* **1988**, *27*, 1101−1104.
(82) Harvey, P. D.; Gray, H. B. *J. Am. Chem. Soc.* **1988**, *110*, 2145−2147.
(83) Mann, K. R.; Thich, J. A.; Bell, R. A.; Coyle, C. L.; Gray, H. B. *Inorg. Chem.* **1980**, *19*, 2462−2468.
(84) Giordano, G.; Crabtree, R. H. *Inorg. Synth.* **1990**, *28*, 88−90.
(85) Zielinska, A.; Skulski, L. *Tetrahedron Lett.* **2004**, *45*, 1087−1089.
(86) Balakrishna, M. S.; Prakasha, T. K.; Krishnamurthy, S. S.; Siriwardane, U.; Hosmane, N. S. *J. Organomet. Chem.* **1990**, *390*, 203−216.
(87) Montalti, M.; Credi, A.; Prodi, L.; Gandolfi, M. T. *Handbook of Photochemistry*, 3rd ed.; Taylor and Francis: Boca Raton, FL, 2006.
(88) Loh, Z.-H.; Miller, S. E.; Chang, C. J.; Carpenter, S. D.; Nocera, D. G. *J. Phys. Chem. A* **2002**, *106*, 11700−11708.
(89) Sheldrick, G. M. *Acta Crystallogr.* **2008**, *A64*, 112−122.
(90) Frisch, M. J. et al. *Gassian 03*, revision C.02; Gaussian, Inc.; Wallingford, CT, 2004.
(91) Becke, A. D. *J. Chem. Phys.* **1993**, *98*, 5648−5652.
(92) Becke, A. D. *Phys. Rev. A: Gen. Phys.* **1988**, *38*, 3098−3100.
(93) Lee, C.; Yang, W.; Parr, R. G. *Phys. Rev. B: Condens. Matter Mater. Phys.* **1988**, *37*, 785−789.
(94) Hehre, W. J.; Radom, L.; Schleyer, P. v. R.; Pople, J. A. *Ab Initio Molecular Orbital Theory*; John Wiley: New York, 1986.
(95) Wedig, U.; Dolg, M.; Stoll, H. *Quantum Chemistry: The Challenge of Transition Metals and Coordination Chemistry*; Springer: Dordrecht, The Netherlands, 1986.
(96) Andrea, D.; Haeussermann, U.; Dolg, M.; Stoll, H.; Preuss, H. *Theor. Chim. Acta* **1990**, *77*, 123−141.
(97) Flükiger, P.; Lüthi, H. P.; Portmann, S.; Weber, J. *MOLEKEL* , 4.3; Swiss Center for Scientific Computing: Manno, Switzerland, 2000; www.cscs.ch/molkel.
(98) Pringle, P. G.; Shaw, B. L. *J. Chem. Soc., Dalton Trans.* **1984**, 849−853.
(99) Langrick, C. R.; Shaw, B. L. *J. Chem. Soc., Dalton Trans.* **1985**, 511−516.
(100) Esswein, A. J.; Dempsey, J. L.; Nocera, D. G. *Inorg. Chem.* **2007**, *46*, 2362−2364.
(101) Cotton, F. A. *Acc. Chem. Res.* **1978**, *11*, 225−232.
(102) Teets, T. S.; Lutterman, D. A.; Nocera, D. G. *Inorg. Chem.* **2010**, *49*, 3035−2043.
(103) Hsu, T.-L. C.; Helvoigt, S. A.; Partigianoni, C. M.; Turró, C.; Nocera, D. G. *Inorg. Chem.* **1995**, *34*, 6186−6190.